

# Spin and pseudospins in layered transition metal dichalcogenides

Xiaodong Xu<sup>1\*</sup>, Wang Yao<sup>2\*</sup>, Di Xiao<sup>3</sup> and Tony F. Heinz<sup>4</sup>

**The recent emergence of two-dimensional layered materials — in particular the transition metal dichalcogenides — provides a new laboratory for exploring the internal quantum degrees of freedom of electrons and their potential for new electronics. These degrees of freedom are the real electron spin, the layer pseudospin, and the valley pseudospin. New methods for the quantum control of the spin and these pseudospins arise from the existence of Berry phase-related physical properties and strong spin–orbit coupling. The former leads to the versatile control of the valley pseudospin, whereas the latter gives rise to an interplay between the spin and the pseudospins. Here, we provide a brief review of both theoretical and experimental advances in this field.**

The investigation of internal quantum degrees of freedom (DoF) of electrons lies at the heart of condensed matter physics. The most-studied example is that of the electron spin, which is associated with a magnetic moment. Its obvious connection with magnetic information storage has led to the vast field of spintronics, which aims to exploit this internal DoF of charge carriers in future electronics<sup>1</sup>. Interest in spin also extends to other binary quantum DoFs of electrons, which may be viewed as pseudospins. Valley pseudospin, which labels the degenerate energy extrema in momentum space, is an example that is often present in periodic solids. Early interest in valley pseudospin dates back to studies in the late 1970s on two-dimensional (2D) electron gases in silicon inversion layers<sup>2–5</sup>, where the roles played by valley degeneracy and inter-valley coupling were examined in various contexts. In particular, theory predicted that, at low densities in the inversion layer, the electron intravalley exchange and correlation could lead to a spontaneous valley polarization—that is, electrons preferentially occupying one valley<sup>4</sup>. In analogy to spin ferromagnetism, this possible formation of ‘valley ferromagnetism’ suggests that the valley pseudospin might also be exploited for non-volatile information storage.

Following the subsequent extensive exploration of spintronics, the parallel concept of valleytronics emerged naturally. Valleytronics aims to use the valley index of carriers to process information<sup>6–11</sup>. This has led to revived interest in valley pseudospin and its control in a number of material systems, including aluminium arsenide quantum wells<sup>6,10,11</sup>, silicon heterostructures<sup>12,13</sup>, diamond<sup>14</sup> and bismuth<sup>15</sup>. Generation of valley current and polarization has been demonstrated in these systems based on the valley-dependent energy dispersion of carriers arising from mass anisotropy. However, the ability to control valley pseudospin has been limited owing to the lack of intrinsic physical properties associated with valley occupancy. This situation stands in contrast to the versatile control available for electron spin, for example, by magnetic fields through the spin magnetic moment, by electric fields through spin–orbit coupling<sup>16</sup>, and by optical fields via spin optical selection rules for interband transitions (Table 1).

The recent discovery of 2D materials<sup>17</sup> such as graphene and transition metal dichalcogenides (TMDs) has provided new opportunities to explore quantum control of valley pseudospin. These 2D materials have a hexagonal lattice structure (Fig. 1a), where valleys of energy–momentum dispersion are generally expected at the corners of the hexagonal Brillouin zone—that is, at the K and –K points (Fig. 1b). In graphene, various schemes have been proposed to generate valley currents using its unique edge modes<sup>7</sup>, defect lines<sup>18</sup>, and strain<sup>19</sup>. The rise of 2D TMDs has significantly advanced the study of valley pseudospin. Following theoretical discoveries of the intrinsic physical properties associated with valley pseudospin<sup>8,9,20</sup>, rapid experimental progress has been made in the control of valley polarization and coherence<sup>21–24</sup> that allows manipulation in ways similar to real spin (Table 1; refs 8,9,20). The present article is motivated by these achievements in 2D TMDs. We briefly introduce the theoretical foundations of valley physics arising from inversion symmetry breaking. We then review the experimental achievements in addressing the valley pseudospin in 2D TMDs, discuss the interplay between spin and valley and layer pseudospins resulting from the strong spin–orbit coupling in TMDs, and consider challenges and future directions.

## Valleytronics in 2D hexagonal lattices

In 2D materials with hexagonal lattice structure, the K and –K valleys are related to one another by time reversal. To manipulate this binary degree of freedom, we need to have measurable physical quantities that distinguish the  $\pm K$  valleys. Such quantities exhibiting valley contrast facilitate operations on information encoded in the valley subspace by coupling to external fields. Take spin as an example. The spin up and down states are time-reversed images of one another and are distinguished by opposite values of magnetic moment. The latter is a pseudovector, possessing odd parity under time reversal. This quantity allows spin to be coupled to magnetic fields and spin polarization to be detected as a magnetization<sup>1</sup>. Physical quantities that have odd parity under time reversal are thus good candidates to distinguish valley pseudospin states.

<sup>1</sup>Department of Physics, Department of Materials Science and Engineering, University of Washington, Seattle, Washington 98195, USA, <sup>2</sup>Department of Physics and Center of Theoretical and Computational Physics, University of Hong Kong, Hong Kong, China, <sup>3</sup>Department of Physics, Carnegie Mellon University, Pittsburgh, Pennsylvania 15213, USA, <sup>4</sup>Departments of Physics and Electrical Engineering, Columbia University, New York, New York 10027, USA.

\* e-mail: xuxd@uw.edu; wangyao@hku.hk

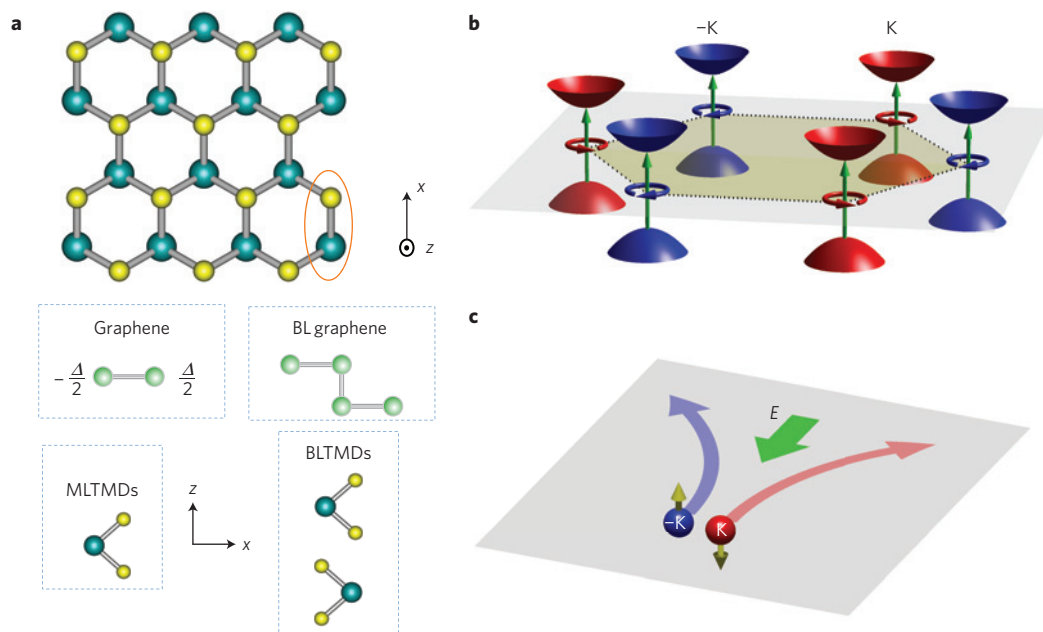


**Figure 1 | 2D hexagonal lattice and valley physics.** **a**, 2D hexagonal lattice, representing graphene, bilayer (BL) graphene, monolayer TMDs (MLTMDs) and bilayer TMDs (BLTMDs). In graphene, inversion symmetry is broken when A and B sublattices have different onsite energies. The MLTMDs have structures that lack inversion symmetry. Inversion symmetry in BL graphene and BLTMDs can be switched on/off by an electric field applied in the  $z$ -direction. **b**, Valley contrasting optical selection rules in a 2D hexagonal lattice with broken inversion symmetry. The interband transition in valley K ( $-K$ ) couples to  $\sigma^+$  ( $\sigma^-$ ) circularly polarized light only (circular arrows). **c**, Valley Hall effect. Blue (red) denotes the electron in valley K ( $-K$ ). The yellow arrows indicate the pseudo-vector quantities (Berry curvature or orbital magnetic moment) of the electron, while the green arrow indicates the applied electric field.

**Table 1 | Internal degree of freedom of Bloch electrons in 2D hexagonal crystals and the associated physical phenomena.**

	Spin	Valley pseudospin	Layer pseudospin
Magnetic moment	✓	✓	
Hall effect	✓	✓	
Optical selection rule	✓	✓	
Electrical polarization			✓

The Berry curvature ( $\Omega$ ) and orbital magnetic moment ( $\mathbf{m}$ ) are two physical quantities that characterize the effect of Berry phase of electrons in the Bloch bands (Box 1; ref. 25).  $\Omega$  gives rise to an anomalous velocity perpendicular to an applied electric field—that is, a Hall effect—whereas  $\mathbf{m}$ , which arises from the self-rotating motion of the electron wavepacket, leads to an energy shift in a magnetic field. As both  $\Omega$  and  $\mathbf{m}$  are pseudovectors, the  $\pm K$  valleys are allowed to have opposite values of these quantities. A conflicting constraint arises when spatial inversion symmetry is present. The spatial inversion operation transforms K and  $-K$  valleys into one another. In the presence of inversion symmetry, the even parity of pseudovectors under the inversion operation requires such quantities to take the same value for states related by inversion. Therefore, inversion symmetry breaking is a necessary condition for the  $\pm K$  valleys to exhibit valley contrast for  $\Omega$  and  $\mathbf{m}$  (refs 8,9).

Two-dimensional group-VIB dichalcogenides  $\text{MX}_2$  ( $M = \text{Mo}$  or  $\text{W}$ ;  $X = \text{S}$  or  $\text{Se}$ ) provide an ideal platform to explore the valley contrasting physics discussed above. In monolayers, the M and X atoms form a 2D hexagonal lattice that lacks spatial inversion symmetry (Fig. 1a). The conduction and valance band edges are at the  $\pm K$  points, formed predominantly by the partially filled  $d$ -orbitals<sup>26</sup> of the M atoms. To first order in  $\mathbf{k}$  (the wavevector measured from  $\pm K$ ) and without the inclusion of spin-orbit

coupling, the two-band  $\mathbf{k} \cdot \mathbf{p}$  Hamiltonian dictated by symmetry is that of a massive Dirac fermion model<sup>20</sup>, namely

$$\hat{H} = at (\tau_z k_x \hat{\sigma}_x + k_y \hat{\sigma}_y) + \frac{\Delta}{2} \hat{\sigma}_z \quad (1)$$

where  $\tau_z = \pm 1$  is the valley index,  $a$  is the lattice constant,  $t$  is the effective nearest neighbour hopping integral, and  $\Delta$  is the bandgap. The Pauli matrix  $\hat{\sigma}$  is defined in a basis consisting of the two  $d$ -orbitals of the M atom, with  $m = 0$  and  $m = 2\tau_z$ . The  $\tau_z$  dependence in equation (1) leads to valley contrast for  $\Omega$  and  $\mathbf{m}$  (Box 2). We note that equation (1) also describes graphene with a staggered sublattice potential (Fig. 1a), the system in which valley contrasting physics was first introduced<sup>8,9</sup>. Such a staggered sublattice potential is naturally realized in silicene<sup>27</sup>, a graphene counterpart with a buckled honeycomb lattice.

In the presence of an in-plane electric field, valley contrasting  $\Omega$  gives rise to a Hall current of the carriers with a sign depending on the valley index (Fig. 1c; refs 8,9,20). This valley Hall effect is an analogue of the spin Hall effect<sup>28–30</sup>. The valley dependence of  $\mathbf{m}$  makes possible the coupling of valley pseudospin to magnetic fields, and the detection of valley polarization as a magnetic signal<sup>8,9</sup>. In principle, this permits the use of valley pseudospin for information processing<sup>31–33</sup>. The valley contrasting  $\mathbf{m}$  is also accompanied by a valley-dependent selection rule for optical excitation with circularly polarized light: the interband transition at K ( $-K$ ) couples only to  $\sigma^+$  ( $\sigma^-$ ) circularly polarized light (Fig. 1b; refs 8,9,20). Such a valley optical selection rule is analogous to the spin optical selection rule in III–V semiconductors. This selectivity allows the optical preparation, control, and detection of valley pseudospin polarization. First-principles calculations for the monolayer  $\text{MoS}_2$  (ref. 23) show that the valley optical selection rule applies not only near K points, but also within a large surrounding region in the Brillouin zone.

The emergence of valley-contrasting physical properties turns out to be a generic consequence of inversion symmetry breaking

**Box 1 | The effect of Berry phase on Bloch electrons.**

Consider a wavepacket of Bloch electrons moving adiabatically in a non-degenerate energy band with index  $n$ . The wavepacket includes a range of wavevectors much smaller than the size of the Brillouin zone, and thus has a real space dimension much larger than the lattice constant. In many situations, it is also possible to have such wavepackets tightly localized compared to the length scale of the external perturbation, so that one can speak simultaneously of the wavevector and the position of the electron. **The equations of motion of Bloch electrons** within this semiclassical picture under applied electric and magnetic fields are

$$\dot{\mathbf{r}} = \frac{1}{\hbar} \frac{\partial E_n(\mathbf{k})}{\partial \mathbf{k}} - \dot{\mathbf{k}} \times \boldsymbol{\Omega}_n(\mathbf{k}), \quad \hbar \dot{\mathbf{k}} = -e\mathbf{E} - e\dot{\mathbf{r}} \times \mathbf{B}$$

where  $\boldsymbol{\Omega}$  is a pseudovector known as the Berry curvature,

$$\boldsymbol{\Omega}_n(\mathbf{k}) = i \frac{\hbar^2}{m^2} \sum_{i \neq n} \frac{\mathbf{P}_{n,i}(\mathbf{k}) \times \mathbf{P}_{i,n}(\mathbf{k})}{[E_n^0(\mathbf{k}) - E_i^0(\mathbf{k})]^2}$$

Here  $\mathbf{P}_{n,i}(\mathbf{k}) \equiv \langle u_{n,\mathbf{k}} | \hat{\mathbf{p}} | u_{i,\mathbf{k}} \rangle$  is the interband matrix element of the canonical momentum operator  $\hat{\mathbf{p}}$ .  $E_n^0(\mathbf{k})$  is the dispersion of the  $n$ th band and  $E_n(\mathbf{k}) = E_n^0(\mathbf{k}) - \mathbf{m}_n(\mathbf{k}) \cdot \mathbf{B}$  is the electron energy,

including the magnetic-field correction. The quantity  $\mathbf{m}$  is also a pseudovector known as the orbital magnetic moment,

$$\mathbf{m}_n(\mathbf{k}) = -i \frac{e\hbar}{2m^2} \sum_{i \neq n} \frac{\mathbf{P}_{n,i}(\mathbf{k}) \times \mathbf{P}_{i,n}(\mathbf{k})}{E_n^0(\mathbf{k}) - E_i^0(\mathbf{k})}$$

The quantities  $\boldsymbol{\Omega}$  and  $\mathbf{m}$  characterize the effect of the Berry phase of electrons in the Bloch bands on their transport properties. In the absence of  $\boldsymbol{\Omega}$  and  $\mathbf{m}$ , the equations of motion reduce to the typical version found in textbooks. **However,  $\boldsymbol{\Omega}$  and  $\mathbf{m}$  become important under some circumstances. For example, consider a 2D crystal with an applied in-plane electric field.** The  $\boldsymbol{\Omega}$  term then corresponds to an anomalous velocity perpendicular to the field—that is, to a Hall effect.  $\boldsymbol{\Omega}$  thus describes the spin Hall effect and the anomalous Hall effect in spin–orbit coupled systems, and the integer quantum Hall effect in magnetic Bloch bands.  $\mathbf{m}$  arises from the self-rotating motion of the electron wavepacket. It is responsible for the anomalous  $g$  factor of electrons in semiconductors: the two Bloch states with opposite spin in a Kramer's pair have opposite values for  $\mathbf{m}$ , which renormalizes the spin Zeeman energy. As evident from their forms, non-zero  $\boldsymbol{\Omega}$  in general implies a finite  $\mathbf{m}$ , and vice versa.

in 2D hexagonal lattices. For example, although graphene bilayers and  $\text{MX}_2$  bilayers are inversion symmetric in their pristine form (Fig. 1a), inversion symmetry can be broken in a controllable way by applying an interlayer bias, which induces a valley-contrasting Berry curvature, magnetic moment, and optical circular dichroism<sup>8,9,34</sup>. These magnetic quantities can be continuously tuned from positive to negative values by the interlayer bias. **This then represents a new type of valley-contrasting magnetoelectric effect in the presence of time reversal symmetry.** For bilayer TMDs, the bandgap at the  $\pm K$  valleys is near the visible regime and independent of the electric field, whereas for bilayer graphene it is in the infrared and changes with electric field<sup>35,36</sup>. Thus bilayer TMDs offer experimental advantages in the exploration of such magnetoelectric effects.

**Progress in the optical control of valley pseudospin**

Experimental breakthroughs in the manipulation of valley pseudospin have been made possible by using monolayer TMDs, which have a direct bandgap at the  $\pm K$  points in the visible wavelength range<sup>37–39</sup>. Photoluminescence (PL) provided the first experimental evidence of the crossover from an indirect bandgap in multilayers to a direct bandgap at the monolayer limit<sup>40,41</sup>. The PL from monolayer  $\text{MoS}_2$  was found to be up to two (four) orders of magnitude larger compared to that from bilayers (bulk crystals). Recent angle-resolved photoemission spectroscopy has directly mapped out the band structure of  $\text{MoS}_2$  (ref. 42) and  $\text{MoSe}_2$  (ref. 43). These studies unambiguously demonstrate the shift of the valence-band maximum from the  $\Gamma$  point for few-layer crystals to the  $K$  points for monolayers, where the hole effective mass is about two-thirds of the free electron mass<sup>44,45</sup>.

Monolayer TMDs with a direct bandgap offer unprecedented opportunities to explore semiconductor optics in the 2D limit. The elementary excitation that plays a key role in optoelectronic phenomena is the exciton, a bound electron and hole pair with an energy spectrum similar to that of a hydrogen atom. In doped semiconductors, a neutral exciton can bind to an extra electron or hole to form a charged exciton (trion), a three-body excited state. Gate-dependent PL and white-light reflection measurements show the evolution from positively charged, to neutral, and then

to negatively charged excitons<sup>24,46,47</sup> as a function of doping level (Fig. 2). **Such electrostatic tunability, even up to room temperature<sup>37</sup>, reflects the strong Coulomb interactions in these materials, which are much more pronounced than in quasi-2D systems such as GaAs quantum wells.** Momentum-resolved luminescence measurements show that the exciton dipole lies in the plane of TMDs (ref. 48). These excitonic transitions in TMDs can be modified by various other external modifications, including gas adsorption<sup>49</sup>, chemical doping<sup>50</sup> and strain effects<sup>51–54</sup>.

The photoluminescence measurements directly reveal the trion binding energy—the energy difference between charged and neutral excitons, with values lying in the range 20–40 meV for different monolayer TMDs (refs 24,46,47). This binding energy is an order of magnitude larger than that in GaAs. The comparable binding energies for positive and negative trions imply comparable electron and hole masses in monolayer TMDs (refs 45,46). Because the binding energy of the neutral exciton is estimated to be approximately ten times that of the trion binding energy<sup>55</sup>, exciton binding energies are expected to be at least a few hundred meV (refs 56–60). Such strong Coulomb interactions reflect the inherent effects of lowered dimensionality, the reduced dielectric screening of an atomically thin material, and the relatively large electron and hole effective masses in these materials. The important role of many-body effects has also been revealed in recent investigations of the ultrafast dynamics of these materials<sup>61–66</sup>.

These robust excitons, consisting of electrons and holes localized in the  $\pm K$  valleys, offer the opportunity to demonstrate the optical manipulation of valley pseudospin. Optical pumping of exciton valley polarization was first demonstrated using polarization-resolved PL (refs 21–23). In these experiments, circularly polarized light selectively excites an electron–hole pair in one valley and the resulting exciton or trion PL is found to be strongly polarized with the same circular polarization as the incident light (Fig. 3a,b, and d,e). This result provides direct evidence that the valley polarization of the photo-excited electrons and holes is largely retained during hot-carrier relaxation, exciton formation, and radiative recombination processes. Intervalley scattering is suppressed by the large momentum separation between valleys, leading to robust valley polarization. In  $\text{MoS}_2$ , PL polarization retention has been

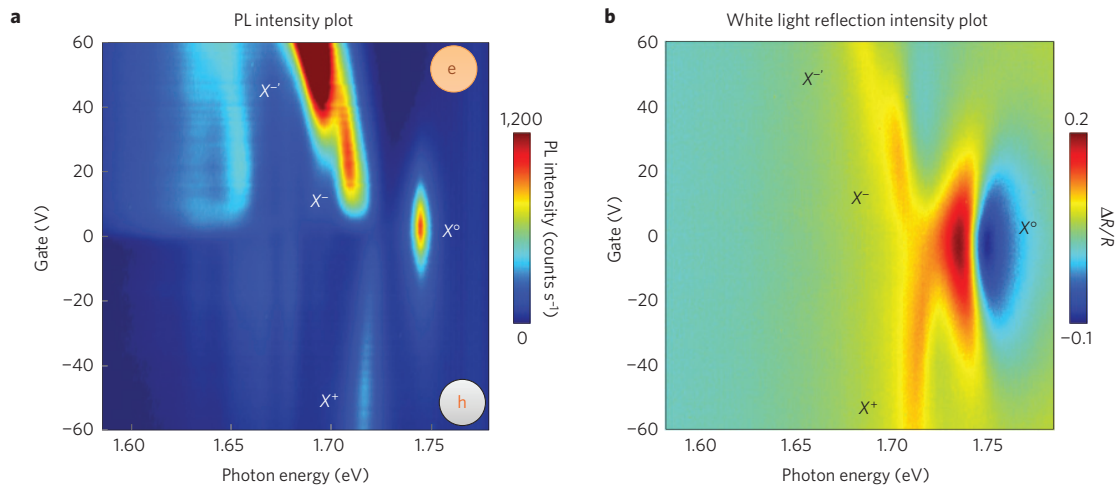


**Figure 2 | Electrostatic charging effects of 2D excitons.** Photoluminescence (PL) (a) and white light reflection (R) intensity plots (b) of monolayer WSe<sub>2</sub> as a function of gate voltage and photon energy at a temperature of 30 K. The electron and hole in a indicate the corresponding carrier doping at positive and negative gate voltages. X<sup>0</sup>: Neutral exciton. X<sup>-</sup> (X<sup>-'</sup>) negatively charged excitons. X<sup>+</sup>: positively charged exciton.

observed to be near unity at low temperature<sup>21,34</sup> and significant even at room temperature<sup>34,62,67</sup>. Valley polarization is also found to have only weak dependence on the photon energy of the exciting light in WSe<sub>2</sub> (ref. 24), consistent with the robustness of the optical selection rule in a large neighbourhood of the  $\pm K$  points<sup>23</sup>.

The Hanle effect can be used to identify whether the polarized PL is due to the polarization of the valley or spin<sup>22</sup>. A transverse magnetic field will cause the spin, but not valley, to precess, and, hence, suppress PL polarization arising from the former, but not from the latter. In monolayer MoS<sub>2</sub>, persistent PL polarization has been observed in transverse magnetic fields up to 9 T (ref. 67), confirming the origin of polarized PL as arising from valley polarization.

The valley optical selection rule also enables the generation and detection of valley coherence. A linearly polarized photon is a coherent superposition of a left and right circularly polarized photon. It can thus transfer optical coherence into excitonic valley coherence. Linearly polarized PL from neutral excitons is observed in monolayer WSe<sub>2</sub>, with a polarization angle that always coincides with that of the linearly polarized excitation (Fig. 3c,f; ref. 24). This implies that the optically generated valley coherence survives through both exciton formation and recombination processes, suggesting a long valley dephasing time.

The optical orientation of excitonic valley pseudospin can be represented using the Bloch sphere (Fig. 3g–i), where the poles correspond to valley polarization and the equator represents an

## Box 2 | Valley physics in a massive Dirac fermion model.

In graphene with a staggered sublattice potential, and in monolayer group VIB transition metal dichalcogenides (TMDs), the conduction and valence band edges at the  $\pm K$  valleys can be described by a massive Dirac fermion model:

$$\hat{H} = at (\tau_x k_x \hat{\sigma}_x + k_y \hat{\sigma}_y) + \frac{\Delta}{2} \hat{\sigma}_z$$

For graphene,  $\hat{\sigma}$  is the Pauli matrix accounting for the A-B sublattice index, whereas for monolayer TMDs,  $\hat{\sigma}$  is the Pauli matrix defined in the basis consisting of the two  $d$ -orbitals of the metal atom with magnetic quantum numbers of  $m = 0$  and  $m = 2\tau_z$ , respectively.

For this massive Dirac fermion model, the Berry curvature in the conduction band is given by

$$\Omega_c(\mathbf{k}) = -\hat{\mathbf{z}} \frac{2a^2 t^2 \Delta}{(4a^2 t^2 k^2 + \Delta^2)^{3/2}} \tau_z$$

where the distribution in the valence band has the same magnitude, but opposite sign. Because of the finite Berry curvature with opposite signs in the two valleys, an in-plane electric field induces a valley Hall effect for the carriers. The orbital magnetic moment has identical values in the conduction and valence bands, which has the form

$$\mathbf{m}(\mathbf{k}) = -\hat{\mathbf{z}} \frac{2a^2 t^2 \Delta}{4a^2 t^2 k^2 + \Delta^2} \frac{e}{2\hbar} \tau_z$$

Its value at the Dirac points ( $k=0$ ) has a simple and suggestive form:  $\mathbf{m} = -\hat{\mathbf{z}} \tau_z \mu_B^*$ , where  $\mu_B^* \equiv e\hbar/2m^*$  resembles the spin Bohr magneton, but with the free electron mass replaced by the effective mass at the band edge. Thus the valley pseudospin is also associated with an intrinsic magnetic moment as far as the low-energy carriers near the band edges are concerned. The valley-dependent  $\mathbf{m}$  makes possible coupling of the valley pseudospin to a magnetic field and the detection of valley polarization as a magnetic signal.

The magnetic moment  $\mathbf{m}$  also gives rise to the circularly polarized optical selection rule for interband transitions, which is generally tied to magnetism. As the two valleys have opposite values of  $\mathbf{m}$ , valley-dependent optical selection rules can be expected. For the massive Dirac fermion model, the Berry curvature, the orbital magnetic moment, and the optical circular dichroism are related by

$$\eta(\mathbf{k}) = -\frac{\mathbf{m}(\mathbf{k}) \cdot \hat{\mathbf{z}}}{\mu_B^*(\mathbf{k})} = -\frac{\Omega_c(\mathbf{k}) \cdot \hat{\mathbf{z}}}{\mu_B^*(\mathbf{k})} \frac{e}{2\hbar} \Delta(\mathbf{k})$$

Here  $\eta(\mathbf{k})$  is the degree of circular polarization for the direct interband transition at  $\mathbf{k}$ , defined as the difference in oscillator strengths for left and right circular polarization normalized by their sum, and  $\Delta(\mathbf{k}) = (4a^2 t^2 k^2 + \Delta^2)^{1/2}$  is the direct transition energy at  $\mathbf{k}$ . At the  $\pm K$  points themselves, we have full selectivity with  $\eta = -\tau_z$ .



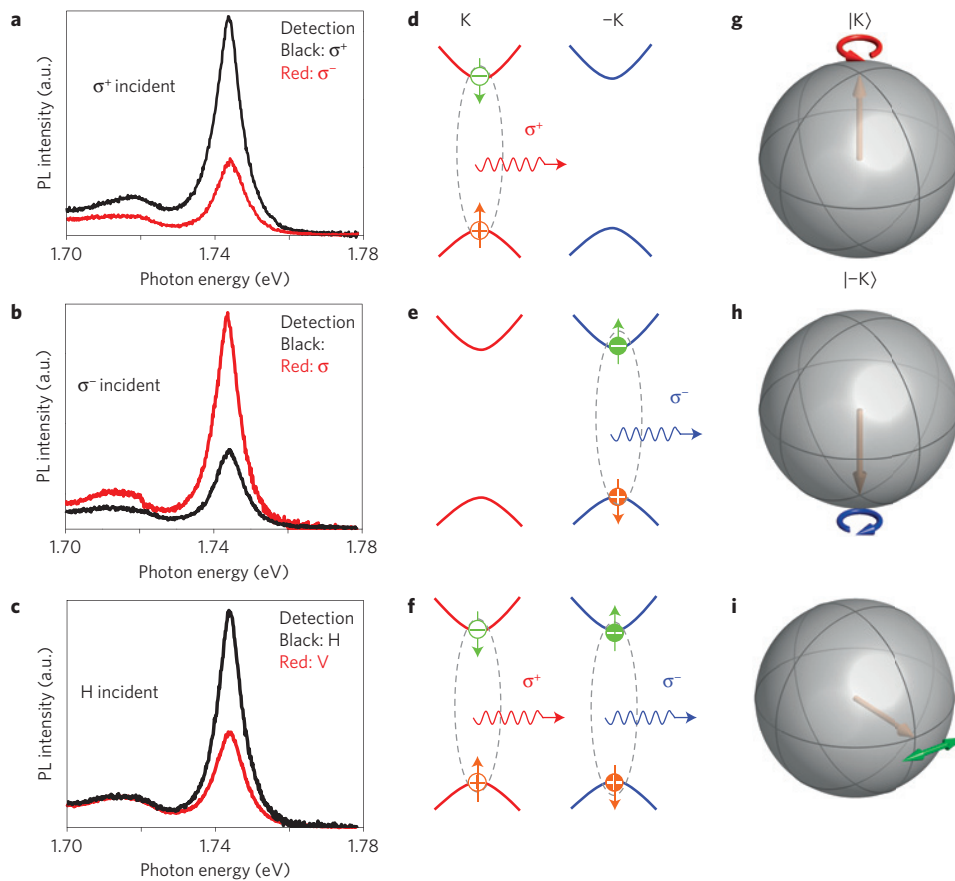


**Figure 3 | Demonstration of valley polarization and valley coherence.** **a–c**, Polarization-resolved photoluminescence of neutral excitons ( $X^0$ ) in monolayer WSe<sub>2</sub> by right ( $\sigma^+$ ) (**a**), left ( $\sigma^-$ ) (**b**) and linearly polarized (**c**) excitations. **d–f**, Energy level diagrams with polarized emission corresponding to **a–c**, respectively. The vertical arrows indicate the spin of the electrons and holes. **g–i**, Bloch vector representations of optical control of valley pseudospin corresponding to **a–c**, respectively. Arrows outside and inside the Bloch sphere correspond to the light polarization and valley pseudospin vectors, respectively.

exciton in an equal, coherent superposition of the two valleys. Experiments have so far demonstrated the addressability of the poles with circular polarized light, and the entire equator with linear polarized light of differing polarization angles. In principle, arbitrary pseudospin vectors pointing away from the equator or poles can be generated using elliptically polarized light.

As well as optical manipulation of valley pseudospin, its electrical control is possible in bilayers, where an out-of-plane electric field can controllably break the inversion symmetry and induce valley contrasting Berry curvature, magnetic moments, and optical selection rules<sup>8,9,68</sup>. This offers the possibility of switching on/off and continuously tuning these properties with reversible electrical control. As initial evidence of the electrical control of valley properties, electrically tunable PL polarization has been observed in bilayer MoS<sub>2</sub> (ref. 68).

### Coupled spin, valley and layer pseudospin physics

The 2D TMDs also provide a unique system to explore the interplay between spin and pseudospins. Strong spin–orbit coupling (SOC) is expected for the band-edge electrons and holes, as they arise from the *d*-orbitals of heavy metal atoms. This SOC takes an unusual form in the multi-valley band structure. In monolayers, the mirror reflection symmetry about the metal atom plane dictates that the spin–orbit splitting is in the out-of-plane direction. Together with time reversal symmetry, the SOC for carriers at the band edge of the  $\pm K$  valleys must take the form

$$\hat{H}_{\text{SOC}} = \lambda \tau_z \hat{S}_z \quad (2)$$

The signature of strong SOC has been observed in optical absorption spectra, where two main excitonic features—the A and B excitons associated with the two spin-split valence bands in the  $\pm K$  valleys<sup>69</sup>—have an energy splitting of 150 meV and 400 meV in molybdenum<sup>41,46</sup> and tungsten dichalcogenides<sup>70,71</sup>, respectively. This splitting agrees with first-principles calculations and ARPES determinations of SOC-induced splitting in the valence bands<sup>42,43</sup>. In contrast to the valence band edges, the conduction band edges are predominantly from the  $m = 0$  *d*-orbitals, for which the onsite SOC vanishes. Nevertheless, first-principles calculations also find a small but finite conduction band spin–valley coupling of the form of equation (2), with a magnitude from several to several tens of meV in different monolayer TMDs (refs 45,59,71–74). This arises primarily from weak mixing of *p*-orbitals from the chalcogen atom and coupling to the remote  $m = 1$  *d*-orbital<sup>75</sup>.

An important consequence of the spin–valley coupling is that the spin index becomes locked with the valley index at the band edges. Consequently, spin can be selectively excited through the valley optical selection rule (Fig. 4a) and intervalley scattering requires a simultaneous spin flip. This affords a protection of both the spin and valley polarization, as intervalley spin relaxation is expected to be slow<sup>73</sup>. Moreover, the generation of the valley Hall effect is accompanied by a spin Hall effect (Fig. 4b; refs 20,76). The spin–valley locking is predicted to qualitatively change the quantum diffusive transport of multivalley massive Dirac fermions<sup>77</sup>.

The coupling between the spin and valley makes possible their interplay with layer pseudospin in AB-stacked bilayer TMDs (ref. 78). In this case, the SOC manifests itself as an out-of-plane spin

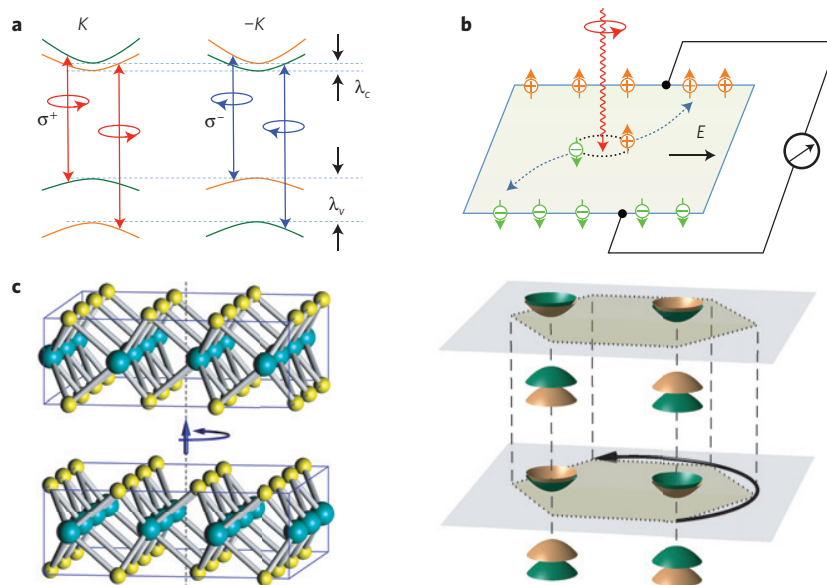


**Figure 4 | Spin, valley, and layer pseudospin coupling.** **a**, Spin and valley coupled optical selection rules in monolayer TMDs.  $\lambda_c$  ( $\lambda_v$ ): spin-orbit coupling induced splitting in conduction (valence) bands. **b**, Hall effect of a photo-carrier injected by circularly polarized light, where the charge Hall current is spin and valley polarized. The blue dashed lines show the trajectories of the electron and the hole. The black arrow indicates the electric field ( $E$ ). **c**, Left: AB-stacked bilayer TMDs, where the two layers are rotated 180° with respect to one another. Right: Valley- and layer-dependent spin splitting. The splitting corresponds to the energy cost for the interlayer hopping that conserves the spin and in-plane momentum, which strongly suppresses hopping. Consequently, band-edge carriers in the  $\pm K$  valleys are mainly localized within an individual layer depending on the spin and valley indices.

splitting, with a sign depending on both valley and layer pseudospins (Fig. 4c). The Hamiltonian near the  $\pm K$  points is then

$$\hat{H}_{\text{Bi}} = \lambda \tau_z \hat{S}_z \hat{\zeta}_z + t_{\perp} \hat{\zeta}_x \quad (3)$$

where  $\hat{\zeta}$  are the Pauli matrices for the layer pseudospin. The first term provides an effective coupling between the spin, valley, and layer pseudospins. The second term describes interlayer hopping that conserves spin and in-plane momentum.

The coupling between spin and pseudospins results in an energy cost ( $\lambda$ ) for interlayer hopping that can be greater than the hopping matrix element  $t_{\perp}$ . This effectively suppresses interlayer hopping at the  $\pm K$  points for both the conduction and valence bands<sup>79</sup>. **The band-edge Bloch wavefunctions are thus predominantly localized in an individual layer**, depending on the spin and valley indices—that is, the spin orientation is locked to layer pseudospin in each valley (Fig. 4c). As the layer pseudospin corresponds to electrical polarization whereas spin and valley pseudospin carry magnetic moments, their coupling gives rise to a number of interesting magnetoelectric effects, such as a valley-dependent spin Zeeman splitting induced by an out-of-plane electric field and spin manipulation conditioned on the valley index<sup>78</sup>.

Evidence of the interplay between spin and pseudospins in 2D TMDs has emerged in recent experiments. Electrical transport measurements of thin-film WSe<sub>2</sub> show a crossover from weak localization to weak antilocalization as a function of vertical electric fields<sup>80</sup>. This observation is ascribed to the electrical modulation of spin Zeeman splitting in the vicinity of the valence-band maxima at the  $\pm K$  points. **Optical measurements demonstrated that the A–B splitting at  $\pm K$  points is nearly independent of the number of layers in tungsten dicalcogenides<sup>71</sup>, evidence of the suppression of interlayer hopping at the  $\pm K$  points because of the strong coupling between the spin, valley, and layer pseudospins (equation (3)).** Localization of the K-point Bloch function to individual layers versus the delocalization of the  $\Gamma$ -point Bloch function is also the reason for the indirect to direct bandgap transition as a function of layer number<sup>81</sup>.

More direct experimental evidence of spin and layer pseudospin coupling is provided by recent polarization-resolved PL studies in bilayer WSe<sub>2</sub> (ref. 79). Strong circularly polarized PL is observed under circularly polarized excitation. This effect is attributed to exciton spin polarization, because valley polarization vanishes in AB-stacked bilayers with inversion symmetry. The large observed exciton spin polarization comes from the long spin relaxation time, which is enhanced by spin–layer locking effects. Interestingly, the trion spectrum splits into a doublet in the presence of large vertical electric fields, and the magnitude of the splitting increases with electrical field (Fig. 5). This splitting arises from the electric-field-induced spin Zeeman splitting due to the spin–layer locking. Furthermore, the trion doublet shows a distinct response to linearly polarized light excitation. The PL of the lower energy trion ( $\omega_2$ ) is not polarized, whereas the other ( $\omega_1$ ) exhibits strong linear polarization, a signature of valley coherence. This observation is spectroscopic evidence of the existence of interlayer and intralayer trion species (Fig. 5).

## Challenges and outlook

Although dynamic control of excitonic valley pseudospin has been demonstrated, **our understanding of the fundamental properties of valley excitons remains incomplete**. One basic quantity, the exciton binding energy, has not yet been established directly by experiment. The binding energy is important for determining other key properties of excitons, including their Bohr radius and many-body interactions with one another. Based on the PL quantum yield and time-resolved PL (refs 21,61,80,82), the lifetime of valley excitons in monolayer TMDs ranges from several to hundreds of picoseconds in different samples. Nonlinear coherent spectroscopy, such as spectral-hole burning, may provide more reliable conclusions on the intrinsic lifetime of excitons. Addressing these fundamental issues is critical for further exploration of valley pseudospin physics.

The robust valley exciton polarization and coherence demonstrated experimentally implies slow valley relaxation and dephasing processes. However, the PL measurement can

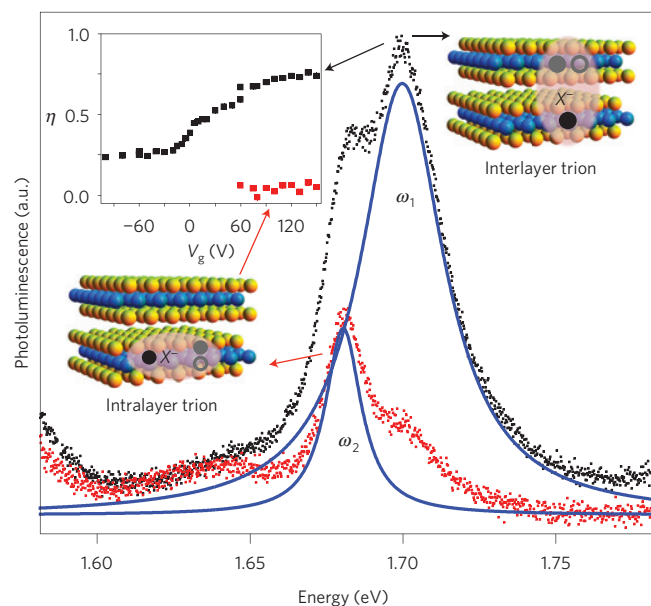


**Figure 5 | Spectroscopic evidence of coupling between spin and layer pseudospin.** Main panel: Polarization-resolved photoluminescence (PL) of bilayer WSe<sub>2</sub> with horizontally polarized excitation and a gate voltage of 150 V. Black dots and red dots are collinear and crossed detection, respectively. The blue lines are a double Lorentzian fit for collinear detection (black dots). The observed trion doublet results from the electric-field-induced spin Zeeman splitting between interlayer and intralayer triions from locking effects between spin and layer pseudospin. Inset: PL from the intralayer trion is unpolarized as valley coherence is suppressed by the exchange coupling with the extra electron, whereas PL from the interlayer trion is strongly polarized in the absence of such exchange coupling, demonstrating optical generation of valley coherence of interlayer trion states.

provide only a lower bound on valley  $T_1$  and  $T_2$  times. Advanced techniques, such as time-resolved measurements and nonlinear optical spectroscopy with valley addressability, are needed to provide these timescales, thus allowing comparison to spin dynamics in materials such as GaAs and Si. At present, knowledge of valley relaxation and decoherence mechanisms is very limited. The various possible mechanisms, including scattering by phonons, impurities, and carrier–carrier interactions need to be systematically addressed through theoretical studies with experimental input.

Valley pseudospin of electrons or holes is a better information carrier compared to short-lived excitons. Success in the optical orientation of excitonic valley pseudospin form the basis for further exploration of the optical manipulation of electron valley pseudospin. Learning from the progress in the optical manipulation of electron spin in III–V materials, we can develop a similar control of valley pseudospin. For example, Kerr and Faraday rotation measurements<sup>83</sup> may be implemented for detecting the electron valley polarization in 2D TMDs. Raman-type optical processes and the a.c. Stark effect<sup>84</sup> may be used for coherent control of electron valley pseudospin via charged valley excitons. Alternatively, the search for the valley and spin Hall effects in transport measurements may reveal the Berry phase physics associated with valleys<sup>85</sup>. Magneto-transport measurements can be performed to determine the valley magnetic moment<sup>86</sup>. To investigate these phenomena, advances in metal contact technology are necessary<sup>87–91</sup>. **Perhaps the most distinctive property of 2D TMDs is the strong coupling between spin and the different pseudospins of carriers<sup>78,79</sup>.** We expect that the interplay between these quantum DoFs in various geometries, including heterostructures<sup>92</sup> and quantum wires<sup>93</sup>, will reveal many novel physical phenomena.

Received 8 January 2014; accepted 10 March 2014;  
published online 30 April 2014

## References

- Wolf, S. A. *et al.* Spintronics: A spin-based electronics vision for the future. *Science* **294**, 1488–1495 (2001).
- J Ohkawa, F. & Uemura, Y. Theory of valley splitting in an N-channel (100) inversion layer of Si III. Enhancement of splittings by many-body effects. *J. Phys. Soc. Jpn* **43**, 925–932 (1977).
- Sham, L., Allen, S., Kamgar, A. & Tsui, D. Valley–valley splitting in inversion layers on a high-index surface of silicon. *Phys. Rev. Lett.* **40**, 472–475 (1978).
- Bloss, W., Sham, L. & Vinter, V. Interaction-induced transition at low densities in silicon inversion layer. *Phys. Rev. Lett.* **43**, 1529–1532 (1979).
- Sham, L. & Nakayama, M. Effective-mass approximation in the presence of an interface. *Phys. Rev. B* **20**, 734–747 (1979).
- Gunawan, O., Habib, B., De Poortere, E. & Shayegan, M. Quantized conductance in an AlAs two-dimensional electron system quantum point contact. *Phys. Rev. B* **74**, 155436 (2006).
- Rycerz, A., Tworzydło, J. & Beenakker, C. W. J. Valley filter and valley valve in graphene. *Nature Phys.* **3**, 172–175 (2007).
- Xiao, D., Yao, W. & Niu, Q. Valley-contrasting physics in graphene: Magnetic moment and topological transport. *Phys. Rev. Lett.* **99**, 236809 (2007).
- Yao, W., Xiao, D. & Niu, Q. Valley-dependent optoelectronics from inversion symmetry breaking. *Phys. Rev. B* **77**, 235406 (2008).
- Bishop, N. *et al.* Valley polarization and susceptibility of composite fermions around a filling factor  $\nu = 32$ . *Phys. Rev. Lett.* **98**, 266404 (2007).
- Shkolnikov, Y., De Poortere, E., Tutuc, E. & Shayegan, M. Valley splitting of AlAs two-dimensional electrons in a perpendicular magnetic field. *Phys. Rev. Lett.* **89**, 226805 (2002).
- Takashina, K., Ono, Y., Fujiwara, A., Takahashi, Y. & Hirayama, Y. Valley polarization in Si(100) at zero magnetic field. *Phys. Rev. Lett.* **96**, 236801 (2006).
- Karch, J. *et al.* Photoexcitation of valley-orbit currents in (111)-oriented silicon metal-oxide-semiconductor field-effect transistors. *Phys. Rev. B* **83**, 121312 (2011).
- Isberg, J. *et al.* Generation, transport and detection of valley-polarized electrons in diamond. *Nature Mater.* **12**, 760–764 (2013).
- Zhu, Z., Collaudin, A., Fauqué, B., Kang, W. & Behnia, K. Field-induced polarization of Dirac valleys in bismuth. *Nature Phys.* **8**, 89–94 (2011).
- Jungwirth, T., Wunderlich, J. & Olejník, K. Spin Hall effect devices. *Nature Mater.* **11**, 382–390 (2012).
- Novoselov, K. S. *et al.* Two-dimensional atomic crystals. *Proc. Natl Acad. Sci. USA* **102**, 10451–10453 (2005).
- Gunlycke, D. & White, C. T. Graphene valley filter using a line defect. *Phys. Rev. Lett.* **106**, 136806 (2011).
- Jiang, Y., Low, T., Chang, K., Katsnelson, M. & Guinea, F. Generation of pure bulk valley current in graphene. *Phys. Rev. Lett.* **110**, 046601 (2013).
- Xiao, D., Liu, G.-B., Feng, W., Xu, X. & Yao, W. Coupled spin and valley physics in monolayers of MoS<sub>2</sub> and other Group-VI dichalcogenides. *Phys. Rev. Lett.* **108**, 196802 (2012).
- Mak, K. F., He, K., Shan, J. & Heinz, T. F. Control of valley polarization in monolayer MoS<sub>2</sub> by optical helicity. *Nature Nanotechnol.* **7**, 494–498 (2012).
- Zeng, H., Dai, J., Yao, W., Xiao, D. & Cui, X. Valley polarization in MoS<sub>2</sub> monolayers by optical pumping. *Nature Nanotechnol.* **7**, 490–493 (2012).
- Cao, T. *et al.* Valley-selective circular dichroism of monolayer molybdenum disulphide. *Nature Commun.* **3**, 887 (2012).
- Jones, A. M. *et al.* Optical generation of excitonic valley coherence in monolayer WSe<sub>2</sub>. *Nature Nanotechnol.* **8**, 634–638 (2013).
- Xiao, D., Chang, M.-C. & Niu, Q. Berry phase effects on electronic properties. *Rev. Mod. Phys.* **82**, 1959–2007 (2010).
- Mattheiss, L. Band structures of transition-metal-dichalcogenide layer compounds. *Phys. Rev. B* **8**, 3719–3740 (1973).
- Ezawa, M. Spin-valley optical selection rule and strong circular dichroism in silicene. *Phys. Rev. B* **86**, 161407 (2012).
- Zhang, F., Jung, J., Fiete, G. A., Niu, Q. & MacDonald, A. H. Spontaneous quantum Hall states in chirally stacked few-layer graphene systems. *Phys. Rev. Lett.* **106**, 156801 (2011).
- Jung, J., Zhang, F., Qiao, Z. & MacDonald, A. H. Valley-Hall kink and edge states in multilayer graphene. *Phys. Rev. B* **84**, 075418 (2011).
- Ezawa, M. Topological Kirchhoff law and bulk-edge correspondence for valley Chern and spin-valley Chern numbers. *Phys. Rev. B* **88**, 161406 (2013).
- Wu, G. Y., Lue, N.-Y. & Chang, L. Graphene quantum dots for valley-based quantum computing: A feasibility study. *Phys. Rev. B* **84**, 195463 (2011).
- Wu, G. Y. & Lue, N.-Y. Graphene-based qubits in quantum communications. *Phys. Rev. B* **86**, 045456 (2012).
- Lee, M.-K., Lue, N.-Y., Wen, C.-K. & Wu, G. Y. Valley-based field-effect transistors in graphene. *Phys. Rev. B* **86**, 165411 (2012).



34. Wu, S. *et al.* Vapor-solid growth of high optical quality MoS<sub>2</sub> monolayers with near-unity valley polarization. *ACS Nano* **7**, 2768–2772 (2013).
35. Zhang, Y. *et al.* Direct observation of a widely tunable bandgap in bilayer graphene. *Nature* **459**, 820–823 (2009).
36. Mak, K., Lui, C., Shan, J. & Heinz, T. Observation of an electric-field-induced band gap in bilayer graphene by infrared spectroscopy. *Phys. Rev. Lett.* **102**, 256405 (2009).
37. Li, T. & Galli, G. Electronic properties of MoS<sub>2</sub> nanoparticles. *J. Phys. Chem. C* **111**, 16192–16196 (2007).
38. Lebegue, S. & Eriksson, O. Electronic structure of two-dimensional crystals from ab initio theory. *Phys. Rev. B* **79**, 115409 (2009).
39. Zhu, Z. Y., Cheng, Y. C. & Schwingenschlögl, U. Giant spin-orbit-induced spin splitting in two-dimensional transition-metal dichalcogenide semiconductors. *Phys. Rev. B* **84**, 153402 (2011).
40. Splendiani, A. *et al.* Emerging photoluminescence in monolayer MoS<sub>2</sub>. *Nano Lett.* **10**, 1271–1275 (2010).
41. Mak, K. F., Lee, C., Hone, J., Shan, J. & Heinz, T. F. Atomically thin MoS<sub>2</sub>: A new direct-gap semiconductor. *Phys. Rev. Lett.* **105**, 136805 (2010).
42. Jin, W. *et al.* Direct measurement of the thickness-dependent electronic band structure of MoS<sub>2</sub> using angle-resolved photoemission spectroscopy. *Phys. Rev. Lett.* **111**, 106801 (2013).
43. Zhang, Y. *et al.* Direct observation of the transition from indirect to direct bandgap in atomically thin epitaxial MoSe<sub>2</sub>. *Nature Nanotechnol.* **9**, 111–115 (2014).
44. Peelaers, H. & Van de Walle, C. G. Effects of strain on band structure and effective masses in MoS<sub>2</sub>. *Phys. Rev. B* **86**, 241401 (2012).
45. Kadantsev, E. S. & Hawrylak, P. Electronic structure of a single MoS<sub>2</sub> monolayer. *Solid State Commun.* **152**, 909–913 (2012).
46. Ross, J. S. *et al.* Electrical control of neutral and charged excitons in a monolayer semiconductor. *Nature Commun.* **4**, 1474 (2013).
47. Mak, K. F. *et al.* Tightly bound trions in monolayer MoS<sub>2</sub>. *Nature Mater.* **12**, 207–211 (2013).
48. Schuller, J. A. *et al.* Orientation of luminescent excitons in layered nanomaterials. *Nature Nanotechnol.* **8**, 271–276 (2013).
49. Tongay, S. *et al.* Broad-range modulation of light emission in two-dimensional semiconductors by molecular physisorption gating. *Nano Lett.* **13**, 2831–2836 (2013).
50. Mouri, S., Miyauchi, Y. & Matsuda, K. Tunable photoluminescence of monolayer MoS<sub>2</sub> via chemical doping. *Nano Lett.* **13**, 5944–5948 (2013).
51. Castellanos-Gomez, A. *et al.* Local strain engineering in atomically thin MoS<sub>2</sub>. *Nano Lett.* **13**, 5361–5366 (2013).
52. Conley, H. J. *et al.* Bandgap engineering of strained monolayer and bilayer MoS<sub>2</sub>. *Nano Lett.* **13**, 3626–3630 (2013).
53. Zhu, C. R. *et al.* Strain tuning of optical emission energy and polarization in monolayer and bilayer MoS<sub>2</sub>. *Phys. Rev. B* **88**, 121301 (2013).
54. He, K., Poole, C., Mak, K. F. & Shan, J. Experimental demonstration of continuous electronic structure tuning via strain in atomically thin MoS<sub>2</sub>. *Nano Lett.* 2931–2936 (2013).
55. Thilagam, A. Two-dimensional charged-exciton complexes. *Phys. Rev. B* **55**, 7804–7808 (1997).
56. Qiu, D. Y., da Jornada, F. H. & Louie, S. G. Optical spectrum of MoS<sub>2</sub>: Many-body effects and diversity of exciton states. *Phys. Rev. Lett.* **111**, 216805 (2013).
57. Feng, J., Qian, X., Huang, C.-W. & Li, J. Strain-engineered artificial atom as a broad-spectrum solar energy funnel. *Nature Photonics* **6**, 866–872 (2012).
58. Shi, H., Pan, H., Zhang, Y.-W. & Yakobson, B. I. Quasiparticle band structures and optical properties of strained monolayer MoS<sub>2</sub> and WS<sub>2</sub>. *Phys. Rev. B* **87**, 155304 (2013).
59. Cheiwchanchamnangij, T. & Lambrecht, W. R. L. Quasiparticle band structure calculation of monolayer, bilayer, and bulk MoS<sub>2</sub>. *Phys. Rev. B* **85**, 205302 (2012).
60. Ramasubramanian, A. Large excitonic effects in monolayers of molybdenum and tungsten dichalcogenides. *Phys. Rev. B* **86**, 115409 (2012).
61. Korn, T., Heydrich, S., Hirmer, M., Schmutzler, J. & Schüller, C. Low-temperature photocarrier dynamics in monolayer MoS<sub>2</sub>. *Appl. Phys. Lett.* **99**, 102109 (2011).
62. Lagarde, D. *et al.* Carrier and polarization dynamics in monolayer MoS<sub>2</sub>. *Phys. Rev. Lett.* **112**, 047401 (2014).
63. Shi, H. *et al.* Exciton dynamics in suspended monolayer and few-layer MoS<sub>2</sub> 2D crystals. *ACS Nano* **7**, 1072–1080 (2013).
64. Sim, S. *et al.* Exciton dynamics in atomically thin MoS<sub>2</sub>: Inter-excitonic interaction and broadening kinetics. Preprint at <http://arxiv.org/abs/1308.2023> (2013).
65. Kumar, N. *et al.* Exciton-exciton annihilation in MoSe<sub>2</sub> monolayers. Preprint at <http://arxiv.org/abs/1311.1079> (2013).
66. Mai, C. *et al.* Many body effects in valleytronics: Direct measurement of valley lifetimes in single layer MoS<sub>2</sub>. *Nano Lett.* **14**, 202–206 (2013).
67. Sallen, G. *et al.* Robust optical emission polarization in MoS<sub>2</sub> monolayers through selective valley excitation. *Phys. Rev. B* **86**, 081301 (2012).
68. Wu, S. *et al.* Electrical tuning of valley magnetic moment through symmetry control in bilayer MoS<sub>2</sub>. *Nature Phys.* **9**, 149–153 (2013).
69. Coehoorn, R., Haas, C. & de Groot, R. Electronic structure of MoSe<sub>2</sub>, MoS<sub>2</sub>, and WSe<sub>2</sub>. II. The nature of the optical band gaps. *Phys. Rev. B* **35**, 6203–6206 (1987).
70. Zhao, W. *et al.* Evolution of electronic structure in atomically thin sheets of WS<sub>2</sub> and WSe<sub>2</sub>. *ACS Nano* **7**, 791–797 (2013).
71. Zeng, H. *et al.* Optical signature of symmetry variations and spin-valley coupling in atomically thin tungsten dichalcogenides. *Sci. Rep.* **3**, 1608 (2013).
72. Košmider, K. & Fernández-Rossier, J. Electronic properties of the MoS<sub>2</sub>-WS<sub>2</sub> heterojunction. *Phys. Rev. B* **87**, 075451 (2013).
73. Song, Y. & Dery, H. Transport Theory of Monolayer Transition-Metal Dichalcogenides through symmetry. *Phys. Rev. Lett.* **111**, 026601 (2013).
74. Kormányos, A. *et al.* *Phys. Rev. B* **88**, 045416 (2013).
75. Feng, W. *et al.* Intrinsic spin Hall effect in monolayers of group-VI dichalcogenides: A first-principles study. *Phys. Rev. B* **86**, 165108 (2012).
76. Liu, G.-B., Shan, W.-Y., Yao, Y., Yao, W. & Xiao, D. Three-band tight-binding model for monolayers of group-VIB transition metal dichalcogenides. *Phys. Rev. B* **88**, 085433 (2013).
77. Lu, H.-Z., Yao, W., Xiao, D. & Shen, S.-Q. Intervalley scattering and localization behaviors of spin-valley coupled Dirac fermions. *Phys. Rev. Lett.* **110**, 016806 (2013).
78. Gong, Z. *et al.* Magnetoelectric effects and valley-controlled spin quantum gates in transition metal dichalcogenide bilayers. *Nature Commun.* **4**, 15 (2013).
79. Jones, A. M. *et al.* Spin-layer locking effects in optical orientation of exciton spin in bilayer WSe<sub>2</sub>. *Nature Phys.* **10**, 130–134 (2014).
80. Yuan, H. *et al.* Zeeman-type spin splitting controlled by an electric field. *Nature Phys.* **9**, 563–569 (2013).
81. Zhao, W. *et al.* Origin of indirect optical transitions in few-layer MoS<sub>2</sub>, WS<sub>2</sub>, and WSe<sub>2</sub>. *Nano Lett.* **13**, 5627–5634 (2013).
82. Van der Zande, A. M. *et al.* Grains and grain boundaries in highly crystalline monolayer molybdenum disulphide. *Nature Mater.* **12**, 554–561 (2013).
83. Kikkawa, J. M. Room-temperature spin memory in two-dimensional electron gases. *Science* **277**, 1284–1287 (1997).
84. Gupta, J. A., Knobel, R., Samarth, N. & Awschalom, D. D. Ultrafast manipulation of electron spin coherence. *Science* **292**, 2458–2461 (2001).
85. Mak, Kin, Fai, McGill, K. L., Park, J. & McEuen, P. L. Observation of the valley Hall effect. Preprint at <http://arxiv.org/abs/1403.5039> (2014).
86. Li, X., Zhang, F. & Niu, Q. Unconventional quantum Hall effect and tunable spin Hall effect in Dirac materials: Application to an isolated MoS<sub>2</sub> trilayer. *Phys. Rev. Lett.* **110**, 066803 (2013).
87. Popov, I., Seifert, G. & Tománek, D. Designing electrical contacts to MoS<sub>2</sub> monolayers: A computational study. *Phys. Rev. Lett.* **108**, 156802 (2012).
88. Radisavljevic, B. & Kis, A. Mobility engineering and a metal-insulator transition in monolayer MoS<sub>2</sub>. *Nature Mater.* **12**, 815–820 (2013).
89. Das, S., Chen, H.-Y., Penumatcha, A. V. & Appenzeller, J. High performance multilayer MoS<sub>2</sub> transistors with scandium contacts. *Nano Lett.* **13**, 100–105 (2013).
90. Fang, H. *et al.* High-performance single layered WSe<sub>2</sub> p-FETs with chemically doped contacts. *Nano Lett.* **12**, 3788–3792 (2012).
91. Baugher, B. W. H., Churchill, H. O. H., Yang, Y. & Jarillo-Herrero, P. Intrinsic electronic transport properties of high-quality monolayer and bilayer MoS<sub>2</sub>. *Nano Lett.* **13**, 4212–4216 (2013).
92. Geim, A. K. & Grigorieva, I. V. Van der Waals heterostructures. *Nature* **499**, 419–425 (2013).
93. Klinovaja, J. & Loss, D. Spintronics in MoS<sub>2</sub> monolayer quantum wires. *Phys. Rev. B* **88**, 075404 (2013).

## Acknowledgements

This work was supported by DoE BES DE-SC0008145 and NSF DMR-1150719 (XX), Croucher Foundation under the Croucher Innovation Award, and the RGC (HKU705513P, HKU8/CRF/11G) and UGC (AoE/P-04/08) of Hong Kong (WY), DoE BES Materials Sciences and Engineering Division (DX), and NSF DMR-1106172 (TH).

## Author contributions

X.X. and W.Y. wrote the paper that was examined and improved by all authors.

## Additional information

Reprints and permissions information is available online at [www.nature.com/reprints](http://www.nature.com/reprints). Correspondence and requests for materials should be addressed to X.X. or W.Y.

## Competing financial interests

The authors declare no competing financial interests.